Title	Rutile TiO2 inverse opal anodes for Li-ion batteries with long cycle life, high-rate capability and high structural stability
Author(s)	McNulty, David; Carroll, Elaine; O'Dwyer, Colm
Publication date	2017-02-14
Original citation	McNulty, D., Carroll, E. and O'Dwyer, C. (2017) 'Rutile TiO2 Inverse Opal Anodes for Li-Ion Batteries with Long Cycle Life, High-Rate Capability, and High Structural Stability', Advanced Energy Materials, 7(12), 1602291 (8pp). doi: 10.1002/aenm.201602291
Type of publication	Article (peer-reviewed)
Link to publisher's version	http://onlinelibrary.wiley.com/doi/10.1002/aenm.201602291/full http://dx.doi.org/10.1002/aenm.201602291 Access to the full text of the published version may require a subscription.
Rights	
Item downloaded from	http://hdl.handle.net/10468/5481

![UCC logo]

**University College Cork, Ireland
Coláiste na hOllscoile Corcaigh**

Rutile TiO$_2$ Inverse Opal Anodes for Li-ion Batteries with Long Cycle Life, High-rate Capability and High Structural Stability

David McNulty[a,b], Elaine Carroll[a,b] and Colm O'Dwyer[a,b,c]*

Dr. David McNulty, Ms. Elaine Carroll, Dr Colm O'Dwyer

[a]Department of Chemistry, University College Cork, Cork T12 YN60, Ireland

[b]Tyndall National Institute, Lee Maltings, Cork T12 R5CP, Ireland

[c]Micro-Nano Systems Centre, Tyndall National Institute, Lee Maltings, Cork T12 R5CP, Ireland

*Email: c.odwyer@ucc.ie; Tel: +353 (0)21 4902732

Abstract

Rutile TiO$_2$ inverse opals provide long cycle life and impressive structural stability when tested as anode materials for Li-ion batteries. The capacity retention of TiO$_2$ IOs is greater than previously reported values for other rutile TiO$_2$ nanomaterials, and the cycled crystalline phase and material interconnectivity is maintained over thousands of cycles. Consequently, this report offers insight into the importance of optimizing the relationship between the structure and morphology on improving electrochemical performance of this abundant and low environmental impact material. TiO$_2$ IOs show gradual capacity fading over 1000 and 5000 cycles, when cycled at specific currents of 75 and 450 mA/g, respectively, while maintaining a high capacity and a stable overall cell voltage. TiO$_2$ IOs achieve a reversible

1

capacity of ~ 170 and 140 mAh/g after the 100th and 1000th cycles respectively, at a specific current of 75 mA/g, corresponding to a capacity retention of ~ 82.4%. The structural stability of the 3D IO phase from pristine rutile TiO_2 to the conductive orthorhombic $Li_{0.5}TiO_2$ is remarkable and maintains it structural integrity. Image analysis shows conclusively that volumetric swelling is accommodated into the predefined pore space, the IO periodicity remains constant and does not degrade over 5000 cycles.

1. Introduction

With the ever advancing improvements in electronics and electrical engineering, never has there been more of a requirement to develop Li-ion battery electrode materials which are able to meet the growing demands for consumer products such as smartphones and tablet computers. Consequently there has been a tremendous amount of effort put into developing materials capable of long cycle-life with suitable stability in capacity, capacity retention and voltage.[1] It is of the utmost importance to identify electrode materials that are capable of delivering stable capacities over a large number of cycles, instead of materials which offer high initial capacities and then significantly fade over the course of a relatively low number of cycles, using eco-friendly and earth-abundant materials. In this vein, from an anode material perspective, alloying materials such as Si and Ge have been the focus of much research in recent years. [2]

TiO₂ has also attracted a lot of attention as an intercalation mode material, being a low voltage insertion host for Li^+ and also as a fast Li^+ insertion/removal host, as well as having low environmental impact and cost.[3] Various polymorphs of TiO_2 have been investigated as an anode material including $TiO_2(B)$, anatase and rutile.[4, 5] The rutile phase of TiO_2 is the most common natural form, as it is the most thermodynamically stable phase under standard conditions. It has previously been reported that Li^+ insertion in rutile TiO_2 is highly

anisotropic, with preferential diffusion occurring along the crystallographic *c* plane rather than along the *ab*-plane.[6] Consequently it is has been shown that the electrochemical behaviour of rutile TiO_2 is greatly dependent on particle size [7]; i.e. having a greater surface area of active material in direct contact with the electrolyte enhances cation diffusion along the *c* plane. Various rutile TiO_2 nanostructures have been reported for application as anode materials such as nanoparticles, nanowires and nanorods.[8-10] Recently inverse opal (IO) structures have proven effective as high performance Li-ion cathode and anode materials due to advantageous properties such as high porosity, thin walls which allow short Li^+ diffusion path lengths and large surface area.[11, 12] In addition to this, the highly ordered, porous, 3D interconnected network, which the IO structure provides, may remove the necessity for binders and conductive additives.[13] We have previously demonstrated the impressive electrochemical performance of IO structured electrode materials with a full Li-ion cell consisting of a Co_3O_4 IO anode and a V_2O_5 IO cathode.[14] This report probes the benefits of the IO structure on the performance of rutile TiO_2 as an excellent and stable Li-ion battery anode.

In this report, we present the formation of a TiO_2 IO material for Li-ion anode applications. XRD, electron diffraction and Raman analysis confirm that the IOs are pure rutile TiO_2. The electrochemical performance of the TiO_2 IOs is evaluated via cyclic voltammetry, rate capability testing and long cycle life galvanostatic tests. The specific capacity results presented in this report, to our knowledge, represent one of the best the electrochemical performances ever reported for rutile TiO_2. We demonstrate stable cycling of TiO_2 IOs over 1000 and 5000 cycles, at specific currents of 75 and 450 mA/g, respectively. The TiO_2 IOs demonstrated excellent Li^+ insertion activity, accommodating up to $Li_{0.50}TiO_2$ and $Li_{0.41}TiO_2$ after 100 and 1000 cycles, respectively, when cycled at a specific current of 75 mA/g. The impressive electrochemical performance of the TiO_2 IOs was achieved in the absence of any binders or various conductive additives. By introducing a high level of order,

the TiO$_2$ IOs showed significantly increased capacity retention values compared to previously reported values for other rutile TiO$_2$ nanostructures.

2. Results and Discussion

2.1 Structural Characterization

TiO$_2$ IO samples were prepared by infilling of a PS sphere template with a TiCl$_4$·2THF precursor solution. Annealing the infilled templates led to thermal decomposition of the sacrificial PS sphere template and the formation of a highly porous crystalline IO network with pore sizes of ~ 400 nm, as shown in the TEM and SEM images shown in **Figure 1**. The walls of the TiO$_2$ IO are comprised of an agglomeration of nanoparticles (NPs) as can be seen in **Figure 1a**, which is similar to our previous work on other TMO IOs prepared from chlorides. [14] The electron diffraction (ED) pattern for a typical TiO$_2$ IO consisted of a series of diffraction rings, indicating its polycrystalline structure, as shown in **Figure 1b**. The ED pattern was successfully indexed to pure rutile TiO$_2$. The porosity of the 3D IO network is evident in the SEM image in **Figure 1c**, layers of IO can be seen in the pores on the surface. The thin walls of the TiO$_2$ IO, the large surface area and the high level of porosity are advantageous from an electrochemical point of view as they provide continuous transport paths for Li ions through the active phase (walls) and the electrolyte phase (pores). [11] The cross-sectional thickness of a typical TiO$_2$ IO was ~ 35.5 µm, as shown in **Figure 1d**. Additional tilted SEM images of TiO$_2$ IOs are shown in **Figure S1**. XRD analysis was used in order to confirm the crystal structure of the TiO$_2$ IO samples. The XRD pattern for a TiO$_2$ IO sample prepared on a stainless steel substrate is shown in **Figure 1e**. The reflections observed can be readily indexed to pure rutile TiO$_2$ (JCPDS No. 00-001-1292) with a *P42/mnm* space group. The additional reflections labelled # are stainless steel peaks from the substrate. From XRD analysis the calculated lattice parameters for our TiO$_2$ IO are *a* ~ 4.62 Å and c ~ 2.93 Å, giving a cell volume of ~ 62.54 Å^3.

2.2 Electrochemical Characterization

Cyclic voltammograms were acquired in order to investigate Li^+ insertion and removal mechanism for the TiO_2 IOs. The 1st, 2nd, 5th and 10th CV scans acquired at a scan rate of 0.1 mV/s are shown in **Figure 2a**. Three reduction peaks were observed in the first cathodic sweep at ~ 2.17, 1.70 and 1.56 V. The broad peak centred at 2.17 V can be attributed to the formation of an SEI layer. The strong reduction peak at 1.70 V and the weaker peak at 1.56 V correspond to the insertion of Li^+ into the rutile TiO_2 structure, i.e. the conversion of TiO_2 into $Li_\chi TiO_2$ ($TiO_2 + \chi Li^+ + \chi e^- \rightarrow Li_\chi TiO_2$). [15] From the second cycle onwards the broad peak at 2.17 V is no longer present in the cathodic scans, indicating that the initial formation of the SEI layer is an irreversible process. A broad peak was observed in the second anodic sweep at ~ 1.47 V, suggesting that after the first cycle an additional Li^+ insertion process occurs at this potential. The main reduction peak shifts slightly from 1.70 V in the first anodic scan to 1.76 V in the tenth anodic scan, this suggests that the insertion of Li^+ into the rutile TiO_2 IO structure is a highly reversible process. It has previously been reported for other rutile TiO_2 nanostructures that the reduction peak at ~1.5 V is only observed in the first anodic sweep and it is no longer observed in subsequent cycles due to an irreversible process occurring during the first cycle. [9, 16] However this peak can be seen in the first 10 cycles for our rutile TiO_2 IOs indicating the structural integrity of the crystal structure of our IO material is maintained and that the insertion and removal of Li^+ into and out of the TiO_2 IO is highly reversible. Three oxidation peaks were observed in the initial anodic sweep. The two broad peaks centred at ~ 1.54 and 1.67 V and the strong peak at 2.00 V correspond to the removal of Li^+ from $Li_\chi TiO_2$. [17] All three cathodic peaks were observed in all of the successive scans, with little variation in peak potentials. The strong oxidation peak observed at 2.00 V in the initial cathodic scan shifted slightly to 2.01 V in the tenth scan.

In order to further evaluate the electrochemical performance, a TiO_2 IO sample was charged and discharged galvanostatically for 1000 cycles using a specific current of 75 mA/g. A series of the resulting charge and discharge curves are shown in **Figure 2b and c**. A weak plateau was observed during the initial charge, from 2.55 – 2.05 V, followed by a stronger plateau from 1.95 – 1.70 V and a sloping region from 1.70 V to the lower potential limit. To further investigate the origin of these plateaux and the sloped region, a differential charge plot was calculated for the first galvanostatic charge curve. Four peaks can be seen in the differential capacity curve as shown in **Figure S2**. The broad peak centred at 2.10 V, the strong peak at 1.74 V and the two weaker peaks at 1.60 and 1.46 V are in excellent agreement with the cathodic peaks observed in the initial cathodic sweep in Figure 2a. The initial charge capacity was ~ 608 mAh/g which is significantly higher than the theoretical capacity for TiO_2 (168 mAh/g for $Li_{0.5}TiO_2$ or 336 mAh/g for Li_1TiO_2). The initial high capacity may be due to defects such as cation vacancies associated with lithiated oxygen sites, which may form during the preparation of the TiO_2 IOs. It has previously been reported that heating transition metal oxides in air can introduce these defects which can serve as additional charge-compensation sites and result in large initial capacities.[18] Consequently, the presence of any such defects may also explain the irreversible capacity loss after the first charge. In addition to this the high initial specific capacity may also be attributed to the formation of an SEI layer.[19] Further to this, specific capacities greater than the theoretical capacity of TiO_2 (168 mAh/g for $Li_{0.5}TiO_2$) have previously been reported over the first 20 cycles for nanocrystalline rutile TiO_2 [17] and over the first 40 cycles for rutile TiO_2 submicroboxes. [5] Yu et al. suggested that the high capacities obtained for the initial cycles may be related to the hollow structure of their submicroboxes, which provides more surface active sites for lithium storage and other irreversible side reactions on nanosized rutile such as the irreversible reaction with residual water.

During the first charge ~ 1.81 mol of Li per TiO_2 unit was inserted into the IO anode and ~ 0.72 mol of Li was removed upon the first discharge, as shown in Figure 2b. This suggests that an irreversible process occurs during the initial charge. The amount of intercalated Li decreased to ~ 0.88 mol after the second charge and decreased further to ~ 0.65 mol after the 10th charge. There was little variation in the number of moles of lithium inserted from the 50th to the 100th charges, decreasing slightly from ~ 0.53 to 0.50 mol, well within the solid solution range for Li_xTiO_2. The voltage profiles from the 200th to the 1000th cycle are smooth curves without any discrete voltage steps as shown in Figure 2c. Previous reports on the galvanostatic response of rutile TiO_2 have suggested that the transition to sloping charge and discharge curves may be attributed to the formation of a nanocomposite consisting of crystalline grains and amorphous regions upon cycling. [7] The effects of cycling on the crystal structure of TiO_2 samples will be discussed in further detail after the electrochemical analysis. There is only a slight difference in the number of moles of lithium inserted from the 200th to the 1000th charges, varying from ~ 0.47 to 0.41 mol, indicating that the insertion and removal of Li^+ is highly reversible, being in the solid solution regime.

The specific capacity values and their related coulombic efficiency values are shown in **Figure 2d**. It is immediately clear the TiO_2 IO anode offers excellent capacity retention over 1000 cycles. The large initial capacities begin to level off after ~ 100 cycles and from this point onwards the capacity retention is exceptionally high. The charge capacity after the 2nd cycle was 295 mAh/g, this decreased to 178 mAh/g after the 50th cycle and to 168 mAh/g after the 100th cycle. There was little variation in the charge capacities from the 100th cycle onwards. The charge capacity varies from 148 to 138 mAh/g after the 500th and 1000th cycles, respectively. The excellent capacity retention is also clear in the coulombic efficiency values. After the first 30 cycles the coulombic efficiency values were > 95% and they remained above this value for the remainder of the 1000 cycles. The specific capacity values obtained for our

TiO_2 IO anodes are higher than other previously reported rutile TiO_2 nanostructures [5, 7, 9, 10, 20] and anatase TiO_2 IOs. [21] To our knowledge our results represent one of the best the electrochemical performances ever reported for rutile TiO_2. A comparison of the charge capacities obtained for other various rutile and anatase TiO_2 nanostructures is presented in **Table S1**. The improved performance may be due to the porous IO structure which can accommodate volume changes due to the insertion and removal of Li^+ as well as offering a large surface area which is in direct contact with the electrolyte. Another impressive attribute of our TiO_2 IO is that they are free of any binders and conductive additives, and are not required for excellent, stable response. The best performing rutile TiO_2 IO anodes are typically conventional slurries [22] and the highly ordered 3D IO structures that spatially confine TiO_2 NP as tightly packed, electrically connected assemblies in a porous structure negated the need for additive or powder composite modifications to maintain or enhance performance.

The capacity retention of TiO_2 IO samples was further investigated by rate capability testing using series of different specific currents ranging from 75 – 450 mAh/g. From the rate-dependent specific capacity data in **Figure 2e**, the TiO_2 IO samples provide outstanding rate capability performance. The specific capacity obtained after 10 cycles at a specific current of 75 mA/g was ~ 196 mAh/g. The average capacity obtained at a specific current of 150 mA/g was ~170 mAh/g, this decreased slightly to 150 mAh/g at 300 mA/g, and decreased slightly further to 137 mAh/g at 450 mA/g. When the specific current was returned to the initial value of 75 mA/g the specific capacity recovered to 165 mAh/g. From the capacity values achieved during the galvanostatic test present in Figure 2d and the rate capability test in Figure 2e it is clear that the rutile TiO_2 materials in IO from demonstrate significant reversible capacity, considerable capacity retention and outstanding rate performance as a macroporous monolithic structure alone. The capacity values obtained are greater than previously reported

values for composites of TiO_2, including composites with graphene and with carbon NPs.[23] Composites with carbon based additives are typically prepared for structures such as nanowires and nanoparticles to increase the conductivity of the active material and to ensure that all regions of the material under investigation are electrochemically active. One of the inherent properties of the IO structure is that it is a highly ordered, porous, 3D interconnected network. This property, which is unique to the IO structure, negates the need to prepare composites to increase conductivity as is demonstrated by the superior capacity values obtained for our TiO_2 IOs compared to previously reported TiO_2 composites.

The rate capability test demonstrates that the TiO_2 IO samples are capable of delivering significantly high capacities even at a high specific current (450 mA/g). In order to further investigate the high rate performance of the TiO_2 IOs, a sample was cycled 5000 times at a specific current of 450 mA/g. A selection of the resulting charge and discharge curves over the course of the 5000 cycles are shown in **Figure 3a, b and c**. During the first charge ~ 0.88 mol of Li per TiO_2 unit was inserted into the IO anode, less than half of the amount inserted during the initial charge at the lower specific current of 75 mA/g (~ 1.81 mol), which is to be expected at a higher specific current. After 100 cycles this value decreased to ~ 0.39 mol and this value did not significantly decrease over the first 1000 cycles, having a value of ~ 0.31 mol after the 1000th charge. After 3000 cycles this value decreased to ~ 0.27 mol and decreased slightly further to ~ 0.21 mol after 5000 cycles. The gradual decrease in the number of moles of intercalated Li over the course of 5000 cycles demonstrates the outstanding reversibility of the Li^+ insertion and removal process for the TiO_2 IO structure.

The specific capacity values obtained over 5000 cycles at a specific current of 450 mA/g and the related coulombic efficiencies are shown in **Figure 3d**. The specific capacity after the 2nd charge was ~ 196 mAh/g and after 100 cycles this decreased to ~ 130 mAh/g. However, after the first 100 cycles the specific capacity values began to level off and the

decrease became far more gradual. After 500 cycles the charge capacity decreased to ~ 110 mA/g and decreased marginally further to ~ 103 mAh/g after 1000 cycles. The gradual decrease in the capacity values resulted in charge capacities of ~ 90 and 76 mAh/g after 2500 and 5000 cycles, respectively. This corresponds to a ~ 26% loss in capacity between the 1000th and 5000th cycles, again demonstrating the impressive stability of the TiO_2 IO structure, particularly when cycled using a large specific current. From the coulombic efficiency values in Figure 3d it can be seen the capacity retention depreciates somewhat after 4000 cycles, however the efficiency never falls below 90%. The average charge capacity over 5000 cycles was ~ 95 mAh/g. Cycling at a specific current of 450 mA/g and obtaining a specific capacity of ~ 100 mAh/g corresponds to a charge time of ~ 13.3 min. Hence, this demonstrates that significantly high specific capacities and capacity retention can be obtained from TiO_2 IOs particularly at fast charging rates. Further, by avoiding definite contribution of carbon additives at potential close approaching 1.0 V, the true response and stability of the rutile 3D IO is demonstrated, with excellent mechanical integrity on current collectors without requiring binders that would clog the open network.

The voltage is very stable over thousands of cycles, maintaining a constant charge-discharge curve shape throughout. Even to a discharge potential of 1.0 V, the TiO_2 IO, this form of TiO_2 maintains a solid solution reaction (never incorporating more than 0.9 mol Li^+) without adverse capacity contribution from electrolyte decomposition. This phase is known to be less of a kinetic hindrance to Li diffusivity, and the nanoparticulate TiO_2 is accessible by cations in 3D without requiring electronic or conductivity shuttling by carbon additives. In its cycled $Li_{\chi=0.3-0.6}TiO_2$ phase, the electronic conductivity is not negatively affected – the voltage stability with cycling is excellent. Previous ab initio calculations on similar phases have shown that the Li 2s electrons are localised to Ti-3d(t_{2g})/4s hybridized sites where ~

10% of the electron density exists in non-localized states, making these compounds very good electronic conductors.[24]

2.3 Post Cycling Structural Characterization

High magnification SEM images of an as-prepared TiO_2 IO sample and IO samples after 100, 1000 and 5000 cycles are shown in **Figure 4a-d**, respectively. The thin walls of the IO and the high degree of porosity of the as-prepared IO can be seen in Figure 4a. After the 100 cycle rate capability test, presented in Figure 2e, the TiO_2 IO does not appear to have undergone any significant structural changes. The walls of the IO after 100 cycles are approximately the same thickness as the as-prepared sample and the pores of the layers underneath the top layer can be seen clearly in Figure 4b. Remarkably, the IO structure was retained even after 1000 and 5000 cycles, as shown in Figure 4c and d, respectively. The walls of the IO have swollen appreciably due to the repeated insertion and removal of Li^+, with the walls of the IO sample after 5000 cycles being slightly thicker than the IO samples after 1000 cycles. Previous reports for TiO_2 have shown a significant structural degradation of nanostructures with repeated cycling.[25] However from Figure 4a-d, it is clear that our TiO_2 IOs have an extremely high level of structural integrity, particularly over a large number of cycles. This is most likely due to the inherent properties of the IO structure. The periodic porous nature of the IO structure allows the walls of the IO to expand into the empty pores, preventing the walls from becoming pulverised and allowing the overall IO structure to be retained. The impressive capacity values of the TiO_2 IOs shown in Figure 2 and 3 and the SEM images after long term cycling, suggest that the IO structure is an ideal structure to optimize the electrochemical performance of rutile TiO_2 by solid solution reactions with Li^+.

Raman spectra for an as-prepared TiO_2 IO sample and IO samples after 100, 1000 and 5000 cycles are shown in **Figure 4e**. The Raman spectrum for an as-prepared TiO_2 IO shows

four Raman-active fundamental modes, as shown in Figure 4e. The B_{1g} (148.9 cm^{-1}), E_g (427.8 cm^{-1}), A_{1g} (606.9 cm^{-1}) and B_{2g} (820.4 cm^{-1}) modes are in excellent agreement with previous reports on other rutile TiO_2 nanostructures [26] and thus confirm that the TiO_2 IOs are pure rutile TiO_2. The two additional peaks in the Raman spectrum at 253.5 and 693.4 cm^{-1} are due to second order scattering features caused by multiple-phonon scattering processes, and they are also considered as characteristic Raman peaks of rutile type TiO_2. [27] The Raman spectra for the TiO_2 IO sample after 100 cycles is a close match with previous reported spectra for orthorhombic $Li_{0.5}TiO_2$. The electrochemical conversion of tetragonal rutile TiO_2 to a orthorhombic lithium titanate (LT) phase during cycling has previously been reported by Laskova et al.[28] The Raman modes at ~ 148.8, 196.7, 245.7, 404.7, 521.8 and 636.4 cm^{-1} correspond to the B_{2g}, B_{3g}, B_{2g}, A_g, B_{2g}, and B_{3g} modes of the LT $Li_{0.5}TiO_2$ phase, respectively.[29] The strongest B_{2g} mode (148.8 cm^{-1}) is red-shifted to lower wavenumbers of ~ 146.5 and 143.9 cm^{-1} after 1000 and 5000 cycles, which is indicative of an increase in particle size. As shown in the SEM images in Figure 4a-d the walls of the IO expand with increased cycling, this increase in thickness may be the cause of the red-shifting. Remarkably, the TiO_2 samples after 1000 and 5000 cycles are still crystalline, which further demonstrates the impressive stability of the TiO_2 IOs as long cycle life anode materials.

To further investigate the conversion from rutile TiO_2 to the orthorhombic LT phase, electron diffraction patterns were acquired for TiO_2 IO samples after 1000 and 5000 cycles, as shown in **Figure 4 f and g**, respectively. The electron diffraction patterns confirm the polycrystalline structure of the material after 1000 and 5000 cycles, with several discrete rings visible in both patterns. The electron diffraction pattern for both samples was successfully indexed to the orthorhombic $Li_{0.5}TiO_2$ phase, which is in excellent agreement with the Raman spectra in Figure 4e and confirms the electrochemical conversion from rutile TiO_2 to the orthorhombic LT phase. Notably, the TiO_2 IO anode material remains crystalline after 1000

cycles, and also after 5000 cycles. While the (200) reflections are slightly more diffuse the (011) reflections are more clearly defined after 5000 cycles. The integrity of both the crystalline phase during reversible Li reactions and also of the 3D macroporous structure, promotes the exceptionally long cycle life and rate-dependent capacity retention. By image analysis (see Supporting Information, **Figure S3**) of the wall and internal pore dimensions, the IO begins to swell isotropically between 100 and 1000 cycles; the IO walls widened from ~ 40 nm to ~ 130 nm, while the voids decreased from ~ 330 nm to ~ 240 nm. After 5000 cycles, the rougher wall maintained uniform swelling with wall and pore dimensions of ~ 160 nm and ~ 210 nm respectively. The periodicity in all cases for as-made TiO_2 and the 3D IO anode cycled up to 5000 times remains constant, confirming that the internal IO porosity accommodated volume changes associated with Li intercalation and crystalline phase change without deterioration of the 3D network.

3. Conclusions

In summary, galvanostatic testing demonstrated the exceptional capacity retention properties of the TiO_2 IOs with rutile crystalline phase, achieving a reversible capacity of ~ 170 and 140 mAh/g after the 100th and 1000th cycles respectively, at a specific current of 75 mA/g. This corresponds to a capacity retention of ~ 82.4% between the 100th and 1000th cycles. The capacity values obtained when cycled 1000 times at a specific current of 75 mA/g are greater than previously reported values for other rutile TiO_2 nanostructures. Crucially, the impressive performance of the TiO_2 IOs was achieved without the need for binders or conductive additives. The superior capacities obtained with the TiO_2 IOs are due to the highly ordered, porous, 3D interconnected network, which is inherent to the IO structure – the reversible intercalation efficiency is noted in the capacity retention, very long cycle life, and also enhanced rate response and voltage stability. Consequently, this report shows how the synergy between defined assembly of rutile TiO_2 nanoparticles as an open-worked 3D

macroporous structure allows a high performance for rutile TiO_2 that typically has a low Li-ion diffusivity within its crystal structure. This abundant source anode material in 3D arranged porous form mitigates performance limitations of some thick composites of active materials, while retaining structural integrity over thousands of cycles.

Previous reports have shown that volume expansion during cycling can lead to substantial capacity fading due to significant changes in nanostructure morphology. However, SEM and TEM images of 3D macroporous TiO_2 IO anodes after 100, 1000 and 5000 cycles demonstrate that the IO structure is retained even after long term cycling at fast charging rates. The porosity of the IO structure is able to accommodate volume changes to TiO_2 nanoparticles that make up the walls of the IO materials, while retaining 3D porous structure and morphology via expansion of the IO walls into the pores. The level of structural integrity retained after 5000 cycles is not only a first for TiO_2 nanostructures but also for nanostructured oxide anode materials in general. The average capacity when cycled at the high specific current of 450 mA/g for 5000 cycles was ~ 95 mAh/g. This shows that significantly high specific capacities can be obtained for TiO_2 IOs over a large number of cycles with exceptional capacity retention, at high specific currents. The impressive electrochemical performance of the rutile phase TiO_2 IOs demonstrates that they are a very promising anode material for long cycle life Li-ion batteries.

4. Experimental Section

Preparation of TiO$_2$ IO

TiO_2 IO samples were prepared *via* infilling of a polystyrene (PS) sphere template. The templates were prepared by drop casting a solution of PS spheres (Polysciences Inc., diameter = 500 nm) in isopropanol (IPA) on to 1 cm^2 pieces of stainless steel; the sphere templates were then infilled with a 0.1 M solution of titanium(IV) chloride tetrahydrofuran complex

($TiCl_4 \cdot 2THF$) in IPA. The infilled sphere templates were heated at 450 °C in air for 1 h, to remove the templates and to crystallize the samples.

Material Characterization

TEM analysis was conducted using a JEOL JEM-2100 TEM operating at 200 kV. SEM analysis was performed using an FEI Quanta 650 FEG high resolution SEM at an accelerating voltage of 10 kV. XRD analysis was performed using a Phillips Xpert PW3719 diffractometer using Cu Kα radiation. (Cu Kα, λ = 0.15418 nm, operation voltage 40 kV, current 40 mA). Raman scattering was performed with a Renishaw InVia Raman Spectrometer using a 30 mW Ar^+ laser at 514 nm excitation. The beam was focused onto the samples using a 50× objective lens and spectra were collected using a RenCam CCD camera.

Electrochemical Characterization

All electrochemical results presented in this report were performed using a BioLogic VSP Potentiostat/Galvanostat. The electrochemical properties of TiO_2 IO samples were investigated in a half cell configuration against a pure Li counter electrode in a two electrode, stainless steel split cell (a coin cell assembly that can be disassembled for post-mortem analysis). The electrolyte used consisted of a 1 mol dm^{-3} solution of lithium hexafluorophosphate salt in a 1:1 (v/v) mixture of ethylene carbonate in dimethyl carbonate with 3 wt% vinylene carbonate. The separator used in all split cell tests was a glass fiber separator (El-Cell ECC1-01-0012-A/L, 18 mm diameter, 0.65 mm thickness). The mass loading for all TiO_2 IO samples was ~ 0.5 – 1.0 mg, no additional conductive additives or binders were added. Cyclic voltammetry was performed using a scan rate of 0.1 mV s^{-1} in a potential window of 3.0 – 1.0 V. Galvanostatic cycling was performed using a range of specific currents (75 – 450 mA/g) in a potential window of 3.0 – 1.0 V. Specific currents of 75 and 450 mA/g correspond to C rates of ~ 0.45 C and 2.68 C, respectively, where 1 C = 168 mAh/g.

WILEY-VCH

Supporting Information

Tilted SEM images of a typical TiO$_2$ IO sample. Differential charge curve for the first charge of a TiO$_2$ IO sample cycled using a specific current of 75 mA/g and image analysis of 3D IO materials isotropic swelling during long term cycling. Table comparing performance of some anatase and rutile TiO$_2$ anodes. Supporting Information is available from the Wiley Online Library or from the author.

Received: ((will be filled in by the editorial staff))

Revised: ((will be filled in by the editorial staff))

Published online: ((will be filled in by the editorial staff))

References

[1]   a) Y. Yao, M. T. McDowell, I. Ryu, H. Wu, N. Liu, L. Hu, W. D. Nix, Y. Cui, *Nano Lett.* **2011**, *11*, 2949; b) Y.-K. Sun, S.-T. Myung, B.-C. Park, J. Prakash, I. Belharouak, K. Amine, *Nat. Mater.* **2009**, *8*, 320; c) J. Luo, J. Liu, Z. Zeng, C. F. Ng, L. Ma, H. Zhang, J. Lin, Z. Shen, H. J. Fan, *Nano Lett.* **2013**, *13*, 6136.

[2]   a) L.-F. Cui, R. Ruffo, C. K. Chan, H. Peng, Y. Cui, *Nano Lett.* **2009**, *9*, 491; b) T. Kennedy, M. Bezuidenhout, K. Palaniappan, K. Stokes, M. Brandon, K. M. Ryan, *ACS Nano*

16

2015, *9*, 7456; c) T. Kennedy, E. Mullane, H. Geaney, M. Osiak, C. O'Dwyer, K. M. Ryan, *Nano Lett.* **2014**, *14*, 716.

[3]   Y. Zhang, Y. Tang, W. Li, X. Chen, *ChemNanoMat* **2016**, *2*, 764.

[4]   a) Y. Tang, Y. Zhang, J. Deng, J. Wei, H. L. Tam, B. K. Chandran, Z. Dong, Z. Chen, X. Chen, *Adv. Mater.* **2014**, *26*, 6111; b) J. Zheng, L. Liu, G. Ji, Q. Yang, L. Zheng, J. Zhang, *ACS Appl. Mater. Interfaces* **2016**, *8*, 20074; c) M. Liu, M. Zhou, H. Yang, G. Ren, Y. Zhao, *Electrochim. Acta* **2016**, *190*, 463; d) L. Kavan, M. Zukalová, M. Kalbáč, M. Graetzel, *J. Electrochem. Soc* **2004**, *151*, A1301.

[5]   X.-Y. Yu, H. B. Wu, L. Yu, F.-X. Ma, X. W. Lou, *Angew. Chem. Int. Ed.* **2015**, *54*, 4001.

[6]   M. V. Koudriachova, N. M. Harrison, S. W. de Leeuw, *Solid State Ion.* **2003**, *157*, 35.

[7]   Y. S. Hu, L. Kienle, Y. G. Guo, J. Maier, *Adv. Mater.* **2006**, *18*, 1421.

[8]   T. Lan, H. Qiu, F. Xie, J. Yang, M. Wei, *Sci. Rep.* **2015**, *5*, 8498.

[9]   Y. Gan, L. Zhu, H. Qin, Y. Xia, H. Xiao, L. Xu, L. Ruan, C. Liang, X. Tao, H. Huang, W. Zhang, *Solid State Ion.* **2015**, *269*, 44.

[10]   H. Qiao, Y. Wang, L. Xiao, L. Zhang, *Electrochem. Commun.* **2008**, *10*, 1280.

[11]   A. Vu, Y. Qian, A. Stein, *Adv. Energy Mater.* **2012**, *2*, 1056.

[12]   a) E. Armstrong, D. McNulty, H. Geaney, C. O'Dwyer, *ACS Appl. Mater. Interfaces* **2015**, *7*, 27006; b) J. H. Pikul, H. Gang Zhang, J. Cho, P. V. Braun, W. P. King, *Nat. Commun.* **2013**, *4*, 1732; c) H. Zhang, X. Yu, P. V. Braun, *Nat. Nanotechnol.* **2011**, *6*, 277.

[13]   M. Osiak, H. Geaney, E. Armstrong, C. O'Dwyer, *J. Mater. Chem. A* **2014**, *2*, 9433.

[14]   D. McNulty, H. Geaney, E. Armstrong, C. O'Dwyer, *J. Mater. Chem. A* **2016**, *4*, 4448.

[15]   P. Kubiak, M. Pfanzelt, J. Geserick, U. Hörmann, N. Hüsing, U. Kaiser, M. Wohlfahrt-Mehrens, *J. Power Sources* **2009**, *194*, 1099.

[16]   G. Liu, S. Zhang, X. Wu, R. Lin, *RSC Adv.* **2016**, *6*, 55671.

[17]   N. A. Milne, M. Skyllas-Kazacos, V. Luca, *J. Phys. Chem. C* **2009**, *113*, 12983.

[18]   K. E. Swider-Lyons, C. T. Love, D. R. Rolison, *Solid State Ion.* **2002**, *152–153*, 99.

[19]   L. Li, Y. Cheah, Y. Ko, P. Teh, G. Wee, C. Wong, S. Peng, M. Srinivasan, *J. Mater. Chem. A* **2013**, *1*, 10935.

[20]   a) Z. Hong, M. Wei, T. Lan, G. Cao, *Nano Energy* **2012**, *1*, 466; b) M. Pfanzelt, P. Kubiak, M. Wohlfahrt-Mehrens, *Electrochem. Solid State Lett.* **2010**, *13*, A91; c) D. Wang, D. Choi, Z. Yang, V. V. Viswanathan, Z. Nie, C. Wang, Y. Song, J.-G. Zhang, J. Liu, *Chem. Mater.* **2008**, *20*, 3435; d) D. Wang, D. Choi, J. Li, Z. Yang, Z. Nie, R. Kou, D. Hu, C. Wang, L. V. Saraf, J. Zhang, I. A. Aksay, J. Liu, *ACS Nano* **2009**, *3*, 907; e) M. Pfanzelt, P. Kubiak, M. Fleischhammer, M. Wohlfahrt-Mehrens, *J. Power Sources* **2011**, *196*, 6815.

[21]   a) J. Jin, S.-Z. Huang, J. Liu, Y. Li, D.-S. Chen, H.-E. Wang, Y. Yu, L.-H. Chen, B.-L. Su, *J. Mater. Chem. A* **2014**, *2*, 9699; b) H. Jiang, X. Yang, C. Chen, Y. Zhu, C. Li, *New J. Chem.* **2013**, *37*, 1578; c) G. Lui, G. Li, X. Wang, G. Jiang, E. Lin, M. Fowler, A. Yu, Z. Chen, *Nano Energy* **2016**, *24*, 72.

[22]   a) J. S. Chen, X. W. Lou, *J. Power Sources* **2010**, *195*, 2905; b) M. Zhen, X. Guo, G. Gao, Z. Zhou, L. Liu, *Chem. Commun.* **2014**, *50*, 11915.

[23]   Z. Zhang, L. Zhang, W. Li, A. Yu, P. Wu, *ACS Appl. Mater. Interfaces* **2015**, *7*, 10395.

[24]   W. J. H. Borghols, D. Lutzenkirchen-Hecht, U. Haake, E. R. H. van Eck, F. M. Mulder, M. Wagemaker, *Phys. Chem. Chem. Phys.* **2009**, *11*, 5742.

[25]   H. Liu, W. Li, D. Shen, D. Zhao, G. Wang, *J. Am. Chem. Soc.* **2015**, *137*, 13161.

[26]   a) S. P. S. Porto, P. A. Fleury, T. C. Damen, *Phys. Rev.* **1967**, *154*, 522; b) P. S. Narayanan, *Proc. Indian Acad. Sci. A* **1950**, *32*, 279; c) V. Swamy, *Phys. Rev. B* **2008**, *77*, 195414.

[27]   a) M. Ye, H.-Y. Liu, C. Lin, Z. Lin, *Small* **2013**, *9*, 312; b) V. Swamy, B. C. Muddle, Q. Dai, *Appl. Phys. Lett.* **2006**, *89*, 163118.

[28]   B. Pitna Laskova, L. Kavan, M. Zukalova, K. Mocek, O. Frank, *Monatsh. Chem.* **2016**, *147*, 951.

[29]   a) L. J. Hardwick, M. Holzapfel, P. Novák, L. Dupont, E. Baudrin, *Electrochimica Acta* **2007**, *52*, 5357; b) R. Baddour-Hadjean, J. P. Pereira-Ramos, M. Smirnov, *Phys. Status Solidi C* **2004**, *1*, 3138; c) R. Baddour-Hadjean, S. Bach, M. Smirnov, J.-P. Pereira-Ramos, *J. Raman Spectrosc.* **2004**, *35*, 577; d) R. Baddour-Hadjean, J. P. Pereira-Ramos, *J. Power Sources* **2007**, *174*, 1188.
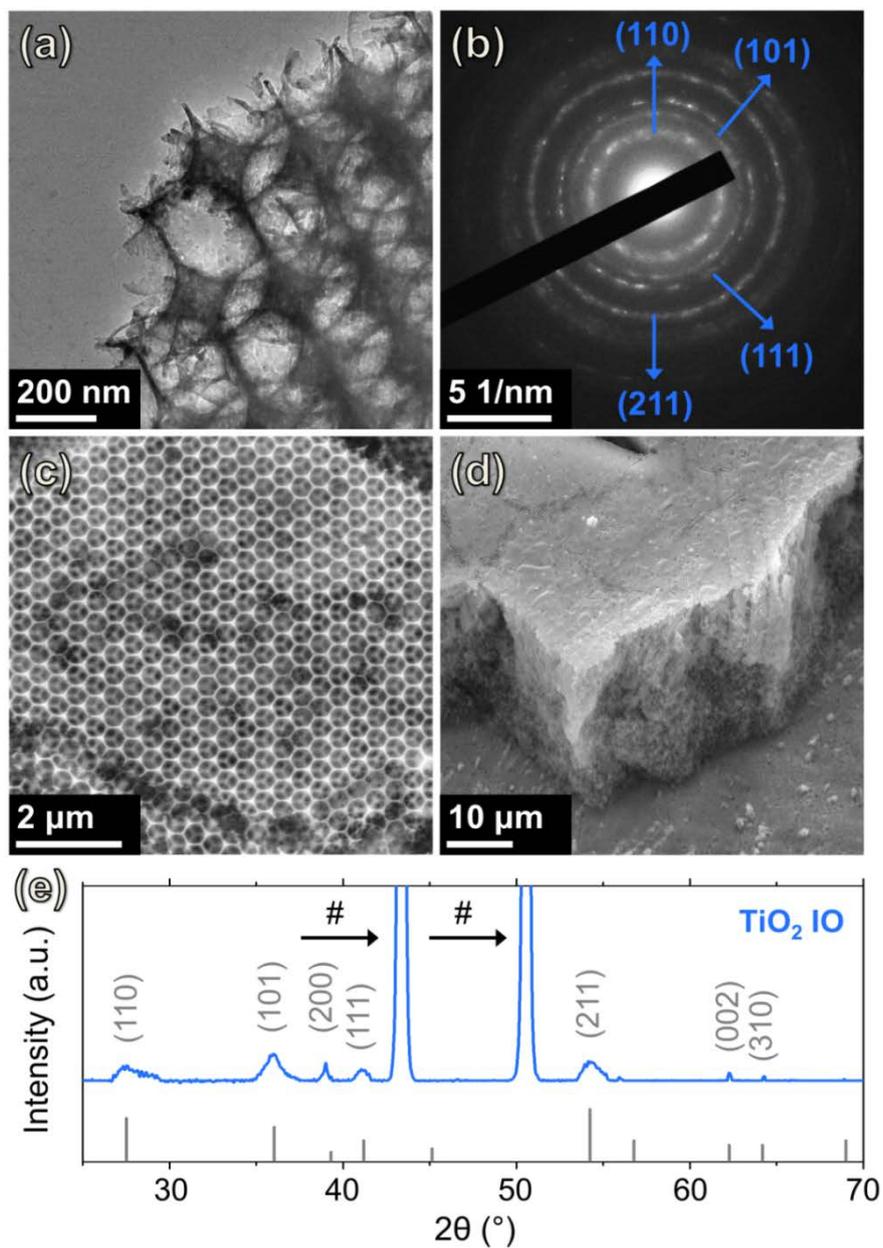
Figure 1. (a) TEM image and (b) electron diffraction pattern of a typical TiO$_2$ IO. SEM images of showing (c) a top down view and (d) the cross-sectional thickness of a typical TiO$_2$ IO. (e) XRD pattern for TiO$_2$ IO prepared on stainless steel substrates (reflections labelled * are stainless steel peaks).
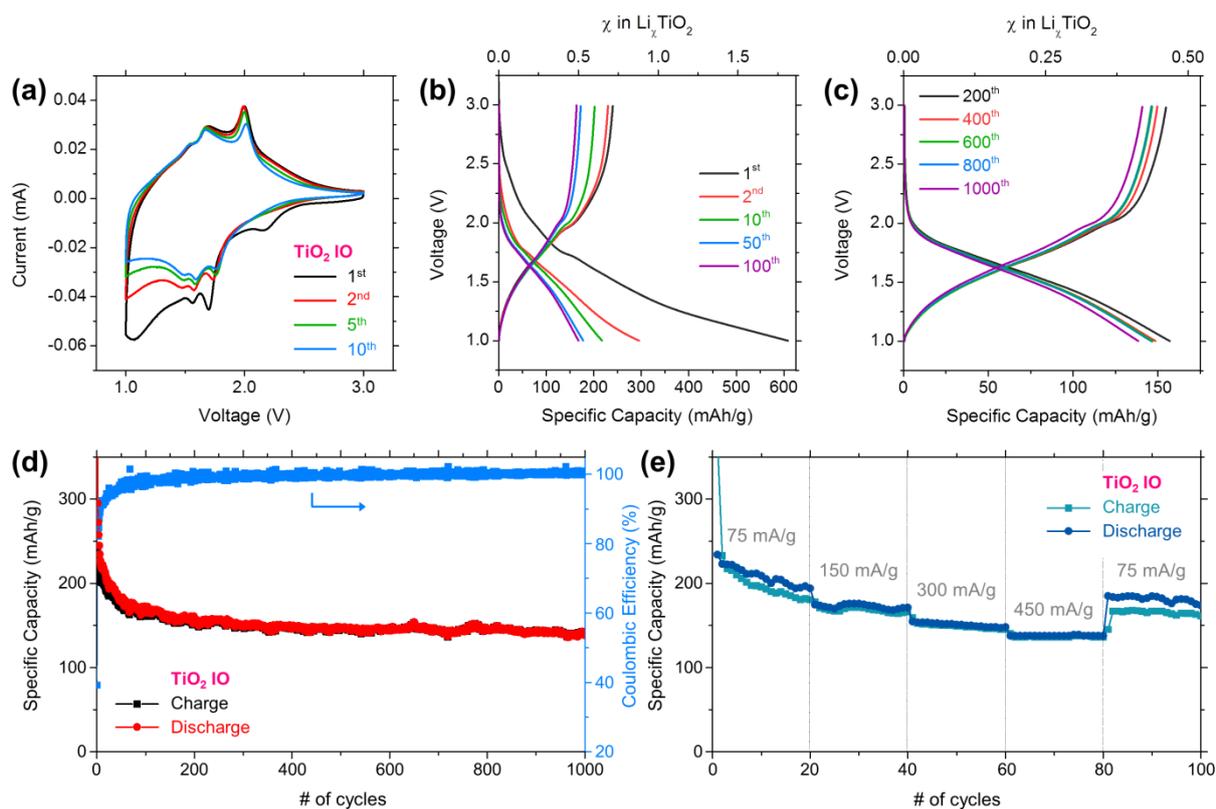
Figure 2. (a) Cyclic voltammograms for TiO$_2$ IO, acquired at a scan rate of 0.1 mV s^{-1}. Charge and discharge voltage profiles for (b) the 1st, 2nd, 10th, 50th and 100th cycles and (c) the 200th, 400th, 600th, 800th and 1000th cycles for TiO$_2$ IO at a specific current of 75 mA/g in a potential window of 3.0 – 1.0 V. (d) Comparison of the specific capacity values and coulombic efficiency obtained for TiO$_2$ IO over 1000 cycles. (e) Rate capability test for TiO$_2$ IO over 100 cycles, using specific currents ranging from 75 to 450 mA/g.
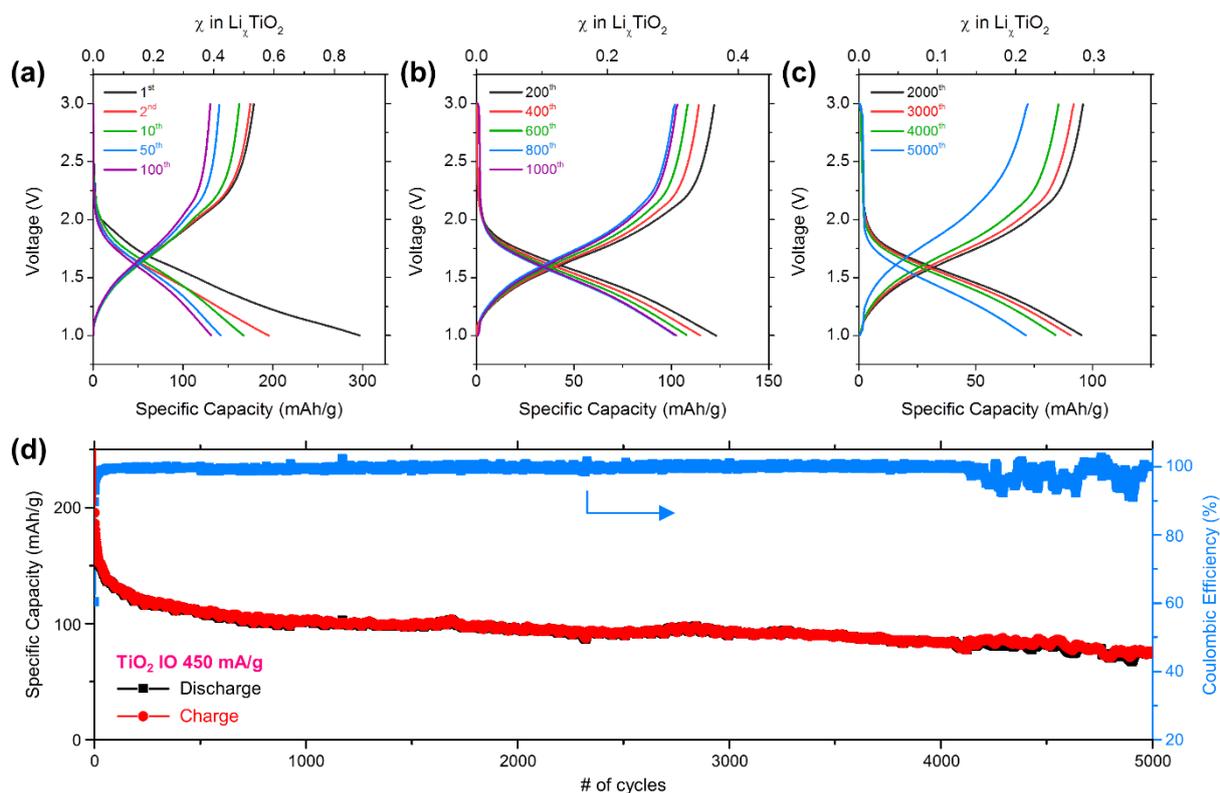
Figure 3. Charge and discharge voltage profiles for (a) the 1st, 2nd, 10th, 50th and 100th cycles, (b) the 200th, 400th, 600th, 800th and 1000th cycles and (c) the 2000th, 3000th, 4000th and 5000th cycles for TiO_2 IO at a specific current of 450 mA/g in a potential window of 3.0 – 1.0 V. (d) Comparison of the specific capacity values and coulombic efficiency obtained for TiO_2 IO over 5000 cycles.
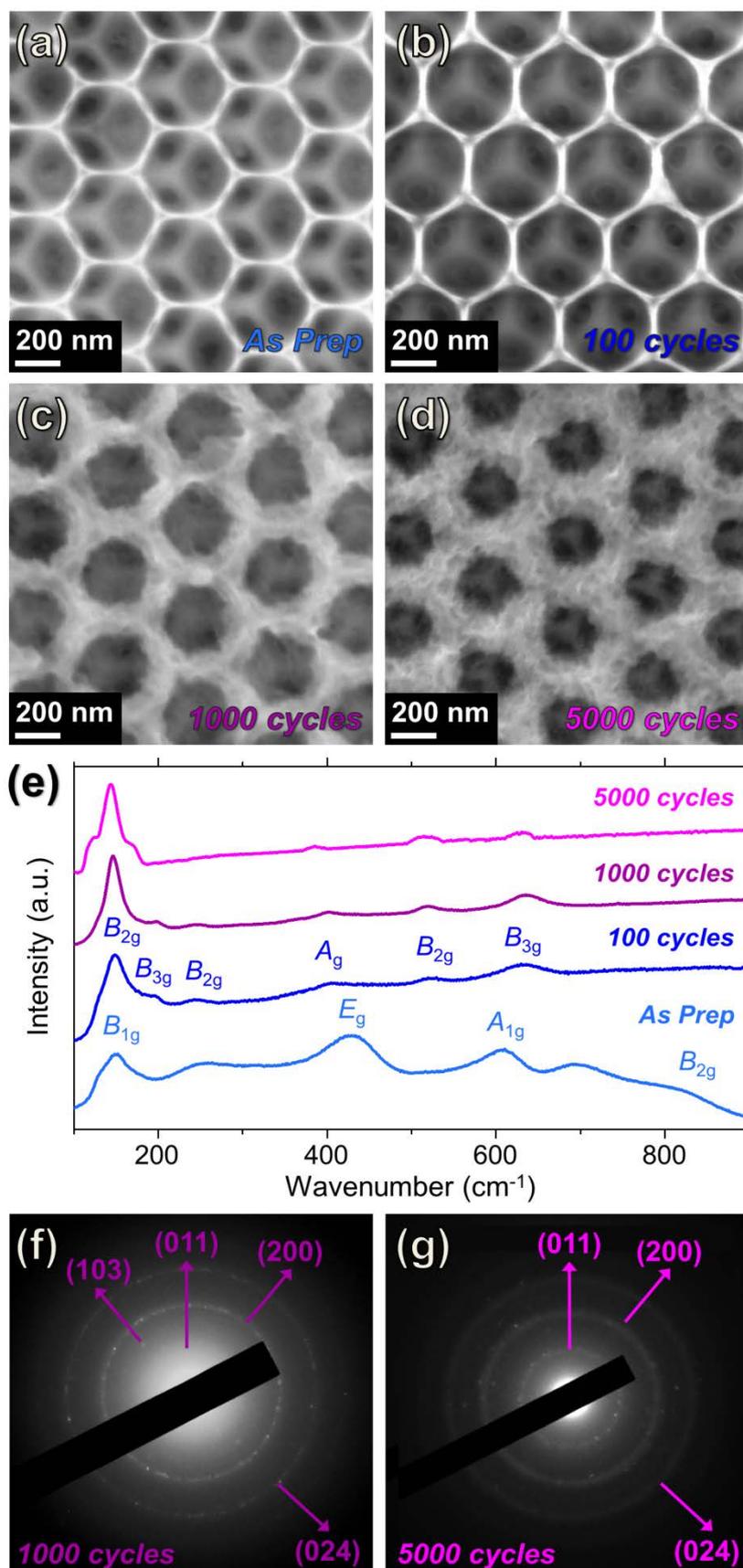
Figure 4. SEM images of (a) an as-prepared TiO$_2$ IO sample and IO samples after (b) 100, (c) 1000 and (d) 5000 cycles. (e) Raman spectrum for an as-prepared TiO$_2$ IO sample and IO samples after cycling. Electron diffraction patterns for Li$_{0.5}$TiO$_2$ IO material after (f) 1000 and (g) 5000 cycles.